ATLAS CONF Note

ATLAS-CONF-2023-057

August 25, 2023

Determining the relative sign of the Higgs boson couplings to W and Z bosons using VBF WH production with the ATLAS detector

The ATLAS Collaboration

Associated production of Higgs and W bosons via vector boson fusion (VBF) offers sensitivity to the relative sign of the Higgs boson couplings to W and Z bosons. In this letter, two searches for this process are presented, using 140 fb^{-1} of proton-proton collision data at $\sqrt{s}$ = 13 TeV recorded by the ATLAS detector at the LHC. The first search targets the scenario with opposite-sign couplings of the W and Z bosons to the Higgs boson, while the second targets the Standard Model-like scenario with same-sign couplings. Both analyses consider Higgs decays to b-quarks and W decays with an electron or muon. The opposite-sign coupling hypothesis is excluded with significance greater than 8σ, and a limit is set on the cross section for VBF WH production of 11.2 times the Standard Model value, compared to an expected limit of 9.4.

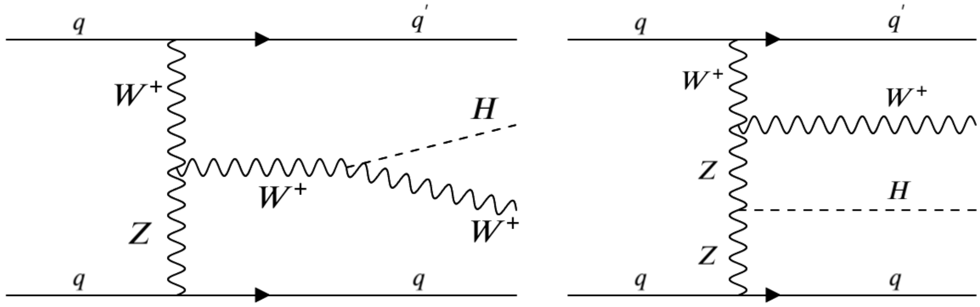

Figure 1: Examples of leading-order Feynman diagrams for VBF WH production, where the Higgs boson interacts with either a W or a Z boson. These diagrams interfere destructively if the Higgs boson couplings to W and Z have the same sign, or constructively if they have opposite sign.

The study of the Higgs boson couplings to W and Z bosons offers a critical means of testing electroweak symmetry breaking in the Standard Model (SM). These couplings can be parametrized in terms of the coupling modifiers κ_W and κ_Z, where a value of 1 corresponds to the SM expectation, or in terms of their ratio $\lambda_{WZ} = \kappa_W/\kappa_Z$ [1]. Any deviation of λ_{WZ} from 1 would indicate a violation of the SM custodial symmetry and be a clear sign for physics beyond the Standard Model (BSM).

By combining measurements of many Higgs boson production and decay modes, the ATLAS [2] and CMS [3] experiments have measured $|\lambda_{WZ}|$ to be consistent with 1 with a precision around 6%. However, this relies primarily on vector boson fusion (VBF) production, WH and ZH associated production, and decays to WW^* and ZZ^*, all of which scale with the square of κ_W or κ_Z. Therefore, the relative sign of these parameters is nearly unconstrained by current measurements, and they are both assumed to be positive in the coupling combinations. Negative values of λ_{WZ} are predicted by various models in which the observed Higgs boson is part of an isospin multiplet larger than a doublet [4], as in the Georgi-Machacek model [5], making an experimental determination of this sign a key priority. In contrast to the current measurements, the VBF WH production mechanism [6] includes diagrams where the Higgs boson couples either to a W or to a Z, as shown in Figure 1. These interfere destructively in the SM, preserving unitarization of longitudinal gauge boson scattering; however, the interference becomes constructive for negative values of λ_{WZ}. This leads to an enhancement in the cross-section, particularly for events with large Higgs or W boson momentum. Therefore, a measurement of this process can be used to exclude the available (κ_W, κ_Z) parameter space with either the same or opposite sign. Furthermore, the enhancement is due to tree-level interference, and therefore does not rely on assumptions regarding BSM loop contributions. Other proposals to measure the sign of λ_{WZ} include exploiting one-loop interference effects in $H \to 4\ell$ [7], or using W^+W^-H production [8].

This note presents two searches for VBF WH production, each using 140.1 ± 1.2 fb^{-1} [9] of pp collision data at $\sqrt{s} = 13$ TeV collected by the ATLAS detector in the years 2015–2018. The first search ("negative λ_{WZ}") targets BSM scenarios with a negative coupling ratio, while the second ("positive λ_{WZ}") targets SM-like production. Both analyses consider the decay modes $H \to b\bar{b}$ and $W \to \ell\nu$, where ℓ is an electron or muon. This leads to a final state with two b-jets, two additional jets from the protons, a charged lepton, and missing transverse momentum ($E_{\mathrm{T}}^{\mathrm{miss}}$) from the neutrino.

The ATLAS experiment [10] at the LHC is a multipurpose particle detector with a forward–backward symmetric cylindrical geometry and a near 4π coverage in solid angle.[1] It consists of an inner detector (ID) for tracking surrounded by a thin superconducting solenoid providing a 2 T axial magnetic field, electromagnetic and hadron calorimeters (ECAL and HCAL), and a muon spectrometer (MS). A two-level trigger system is used to select events. The first-level trigger is implemented in hardware and uses a subset of the detector information to accept events at a rate below 100 kHz. This is followed by a software-based trigger that reduces the accepted event rate to 1 kHz on average depending on the data-taking conditions. An extensive software suite [11] is used in data simulation, in the reconstruction and analysis of real and simulated data, in detector operations, and in the trigger and data acquisition systems of the experiment.

The VBF WH process is simulated at leading-order accuracy in α_S with MadGraph5_aMC@NLO [12] for the matrix element (ME) calculation, interfaced to Pythia 8 [13] for parton shower (PS), hadronization, and multiple parton interactions. The NNPDF3.0nlo parton distribution function (PDF) set is used [14]. Predictions are obtained for various values of κ_W and κ_Z using the procedure outlined in Ref. [6]. Only real values of the κ parameters are considered, as complex values lead to an unphysical model. The largest backgrounds come from $t\bar{t}$, W+jets, and Wt single-top production, with smaller contributions from t- and s-channel single-top, Z+jets, VV, VH, $t\bar{t}H$, and $t\bar{t}V$ production ($V = W$ or Z). Backgrounds from $t\bar{t}$ and single top quark production are simulated with Powheg [15, 16] interfaced to Pythia8. Overlap between Wt and $t\bar{t}$ production is handled using the Diagram Removal (DR) scheme [17]. The W+jets and Z+jets processes are simulated with Sherpa 2.2.1 [18] for ME and PS. The merging of different parton multiplicities is achieved through the CKKW-L [19] technique. Electroweak production of WZ plus two jets is simulated at leading order with MadGraph5_aMC@NLO interfaced to Pythia8. Other VV processes are simulated with Sherpa, version 2.2.1 for quark-initiated processes and 2.2.2 for gluon-initiated processes. Other Higgs boson processes are generated with Powheg, with the MiNLO procedure [20] applied for quark-induced VH, and use Pythia8 for the parton shower. The $t\bar{t}V$ process is simulated at NLO with MadGraph5_aMC@NLO interfaced to Pythia8. The background from events with misidentified or non-prompt leptons is evaluated by extrapolating from a region with inverted lepton isolation requirements, and it is determined to be negligible.

Events in the electron channel were selected online using a single-electron trigger. In the muon channel, events with the vector sum of the offline $E_{\mathrm{T}}^{\mathrm{miss}}$ and of the muon p_{T} greater than 150 GeV were selected with an $E_{\mathrm{T}}^{\mathrm{miss}}$ trigger, while below this threshold a single-muon trigger was used.[2] Due to the changing beam conditions, the kinematic and isolation requirements on the trigger objects varied throughout the data-taking period. Electrons are reconstructed offline by matching clusters of energy deposits in the ECAL to tracks in the ID, which are re-fit to account for energy loss due to bremsstrahlung [21]. Events in the electron channel must have one electron candidate with $p_{\mathrm{T}} > 27$ GeV and $|\eta| < 2.47$ passing the *Tight* likelihood identification criteria and the *HighPtCaloOnly* isolation criteria of Ref. [21]. The electron must furthermore be associated to the primary vertex[3] by requiring $|d_0|/\sigma_{d_0} < 5$ and $|z_0 \sin(\theta)| < 0.5$ mm, where d_0 is the track's transverse impact parameter, σ_{d_0} is its uncertainty, and z_0 is the longitudinal impact parameter. Muons are reconstructed offline by matching tracks in the ID and MS, accounting for energy loss

[1] ATLAS uses a right-handed coordinate system with its origin at the nominal interaction point (IP) in the center of the detector and the z-axis along the beam pipe. The x-axis points from the IP to the centre of the LHC ring, and the y-axis points upwards. Polar coordinates (r, ϕ) are used in the transverse plane, ϕ being the azimuthal angle around the z-axis. The pseudorapidity is defined in terms of the polar angle θ as $\eta = -\ln\tan(\theta/2)$ and is equal to rapidity $y = 0.5\ \ln((E + p_z)/(E - p_z))$ in the relativistic limit. Angular distance is measured in units of $\Delta R \equiv \sqrt{(\Delta y)^2 + (\Delta\phi)^2}$. The transverse momentum is defined as $p_{\mathrm{T}} = \sqrt{p_x^2 + p_y^2}$.

[2] The trigger-level $E_{\mathrm{T}}^{\mathrm{miss}}$ calculation does not include muons, making this vector sum a close approximation of the trigger-level $E_{\mathrm{T}}^{\mathrm{miss}}$.

[3] The primary vertex is taken as the vertex with the highest sum of squared transverse momenta of associated tracks.

in the calorimeters [22]. Events in the muon channel must have one muon satisfying $p_{\mathrm{T}} > 25$ GeV (27 GeV) if an $E_{\mathrm{T}}^{\mathrm{miss}}$ (single-muon) trigger was used, $|\eta| < 2.5$, *Medium* quality, and *HighPtTrackOnly* isolation, as defined in Ref. [22]. Similar to electrons, the track must satisfy $|d_0|/\sigma_{d_0} < 3$ and $|z_0 \sin(\theta)| < 0.5$ mm. In both channels, events are rejected if a second lepton is present. For this veto, the p_{T} requirement is lowered to 7 GeV, *Loose* identification and isolation requirements are applied, and the muon pseudorapidity range is widened to $|\eta| < 2.7$.

Jets are reconstructed from particle flow objects [23], combined using the anti-k_t [24] algorithm with a radius parameter of 0.4. Jets in the central region ($|\eta| < 2.5$) must have $p_{\mathrm{T}} > 20$ GeV, while the p_{T} requirement is raised to 30 GeV for forward jets ($2.5 < |\eta| < 4.5$). To reduce the effect of multiple collisions per bunch crossing, jets in the central (forward) region with $p_{\mathrm{T}} < 60$ GeV (120 GeV) must have a jet vertex tagger [25] score > 0.5 (forward jet vertex tagger [26] score < 0.5). Jets in the central region may be identified as containing the decay of a b-hadron (b-tagged) using a combination of information including secondary vertex reconstruction, track impact parameter, and decay-chain fitting. The deep-learning algorithm DL1r [27, 28] is used, with a working point which has 70% efficiency for b-jets from top quark decays. In addition to the standard jet calibration [23], two corrections are applied to b-jets to improve their energy resolution [29]. First, if any *Medium* [22] muons with $p_{\mathrm{T}} > 5$ GeV and $|\eta| < 2.5$ are found within a p_{T}-dependent cone around the jet axis, the four-momentum of the closest muon is added to that of the jet. In addition, a residual correction is applied to equalize the response to jets with leptonic or hadronic decays of heavy-flavour hadrons. The $E_{\mathrm{T}}^{\mathrm{miss}}$ is calculated as the negative vector sum of the transverse momenta of all jets and leptons in the event, in addition to a track-based soft term [30].

Events must have exactly one lepton, exactly two b-tagged jets, and at least two non-tagged jets. The two non-tagged jets with the highest p_{T} are chosen as the VBF jets, and events are required have a rapidity separation of $|\Delta y_{jj}| > 3$ between them. After these requirements, approximately 430,000 background events are expected from simulation, primarily $t\bar{t}$, compared to 860 signal events if $\kappa_W = 1$ and $\kappa_Z = -1$, or 50 if both parameters are 1. Numerous kinematic variables are used to improve the signal-to-background ratio. These include the VBF jets' invariant mass m_{jj} and rapidity separation $|\Delta y_{jj}|$, as well as the b-jets' invariant mass $m_{b\bar{b}}$, transverse momentum $p_{\mathrm{T}}^{b\bar{b}}$, and $\Delta R_{b\bar{b}}$. The W boson is reconstructed by four-momentum addition of the lepton and neutrino, where the neutrino is assumed to have p_{T} equal to the $E_{\mathrm{T}}^{\mathrm{miss}}$ and η equal to that of the charged lepton. This is used to calculate the leptonic top quark mass $m_{\mathrm{top}}^{\mathrm{lep}}$, the centrality $\xi_{Wb\bar{b}}$, and $\Delta\phi(Wb\bar{b}, jj)$, according to the definitions in Table 1. Finally, $N_{\mathrm{jets}}^{\mathrm{veto}}$ is defined as the number of jets with $p_{\mathrm{T}} > 25$ GeV and $|\eta| < 2.5$ which are not VBF or b-tagged jets. In the negative λ_{WZ} analysis, a single signal region denoted SR^- is used, while the positive λ_{WZ} analysis uses two orthogonal regions, $\mathrm{SR}^+_{\mathrm{loose}}$ and $\mathrm{SR}^+_{\mathrm{tight}}$, to enhance the sensitivity to the smaller SM signal. The selection criteria that define these regions are given in Table 1; they were chosen to maximize the statistical significance, while keeping enough simulated events for a robust determination of the backgrounds and the systematic uncertainties. Compared to the negative λ_{WZ} signal, the SM signal has lower Higgs boson p_{T}, but similar VBF jet p_{T} and additional jet activity. This motivates the tighter cut on $p_{\mathrm{T}}^{b\bar{b}}$ in SR^-, and the cuts on m_{jj} and $N_{\mathrm{jets}}^{\mathrm{veto}}$ in $\mathrm{SR}^+_{\mathrm{loose}}$ and $\mathrm{SR}^+_{\mathrm{tight}}$.

In order to improve the background estimation, control regions (CRs) are defined for $t\bar{t}$, W+jets, and Wt, separately for the two analyses. The CRs are dominated by the target background and depleted of signal, while maintaining key kinematic features of the SRs. The $t\bar{t}$ CRs use the high $m_{b\bar{b}}$ sideband, and consider values of $|\Delta y_{jj}|$ or m_{jj} that are lower than in the SRs. The $t\bar{t}$ events with high $m_{\mathrm{top}}^{\mathrm{lep}}$ often have a misidentified charm jet in place of the leptonic top's b-jet; to preserve this feature, the $t\bar{t}$ CRs also include a lower cut on this variable. The W CRs use a 2-dimensional cut on $\Delta R_{b\bar{b}}$ and $p_{\mathrm{T}}^{b\bar{b}}$ to find events where the b-jets are too close together to be consistent with the Higgs boson mass. The Wt CRs use high values

Table 1: Definition of the signal regions used in the analyses. The SRs for the positive λ_{WZ} analysis are orthogonal: events in $\mathrm{SR}^+_{\mathrm{tight}}$ are excluded from $\mathrm{SR}^+_{\mathrm{loose}}$. The definition of the W boson system is given in the text.

Variable	Description	SR^-	$\mathrm{SR}^+_{\mathrm{loose}}$	$\mathrm{SR}^+_{\mathrm{tight}}$
$m_{b\bar{b}}$	Invariant mass of the two b-jets ($b\bar{b}$ system).	$\in (105, 145)$ GeV	$\in (105, 145)$ GeV	$\in (105, 145)$ GeV
$\Delta R_{b\bar{b}}$	ΔR between the two b-jets.	< 1.2	< 1.6	< 1.2
$p_{\mathrm{T}}^{b\bar{b}}$	p_{T} of the $b\bar{b}$ system.	> 250 GeV	> 100 GeV	> 180 GeV
m_{jj}	Invariant mass of the VBF jets.	–	> 600 GeV	> 1000 GeV
$\lvert\Delta y_{jj}\rvert$	Rapidity separation of the VBF jets.	> 4.4	> 3.0	> 3.0
$m_{\mathrm{top}}^{\mathrm{lep}}$	Invariant mass of the W and either b-jet which is closest to 172.7 GeV.	> 260 GeV	> 260 GeV	> 260 GeV
$\xi_{Wb\bar{b}}$	$\frac{\lvert y_{Wb\bar{b}} - y_{jj}\rvert}{\lvert\Delta y_{jj}\rvert}$, where $y_{Wb\bar{b}}$ and y_{jj} are the rapidity of the $Wb\bar{b}$ system and the VBF-jet system.	< 0.3	< 0.3	< 0.3
$\Delta\phi(Wb\bar{b}, jj)$	Azimuthal separation between the $Wb\bar{b}$ system and the VBF-jet system.	–	–	> 2.7
$N_{\mathrm{jets}}^{\mathrm{veto}}$	Number of non-tagged, non-VBF jets with $p_{\mathrm{T}} > 25$ GeV and $\lvert\eta\rvert < 2.5$.	–	≤ 1	$= 0$

of $\Delta R_{b\bar{b}}$ to remove signal, and high values of $m_{\mathrm{top}}^{\mathrm{lep}}$ and W boson p_{T} to reduce the contamination from $t\bar{t}$ events. The full definitions of these CRs are given in Table 2. For each analysis, the signal region(s) and the CRs are used together in a binned profile likelihood fit [31] [32]. The number of events in each region is taken as the observable. The normalization of each of the main backgrounds is determined with an unconstrained parameter in the fit, $k_{t\bar{t}}$, k_W, or k_{Wt}, while systematic uncertainties are treated as nuisance parameters with gaussian constraints.

Table 2: Definitions of the control regions for $t\bar{t}$, W+jets, and Wt. The W boson transverse momentum p_{T}^{W} is the vector sum of the lepton p_{T} and $E_{\mathrm{T}}^{\mathrm{miss}}$; the W boson transverse mass is calculated as $m_{\mathrm{T}}^{W} = \sqrt{2\, E_{\mathrm{T}}^{\mathrm{miss}}\, p_{\mathrm{T}}^{\ell}\, (1 - \cos\phi)}$, where ϕ is the azimuthal angle between the lepton and $E_{\mathrm{T}}^{\mathrm{miss}}$; p_{T}^{j1} is the p_{T} of the leading VBF jet. Other variables are defined in Table 1.

Variable	$t\bar{t}$ CR$^-$	$t\bar{t}$ CR$^+$	W+jets CR$^-$	W+jets CR$^+$	Wt CR$^-$	Wt CR$^+$
$m_{b\bar{b}}$	> 145 GeV	> 145 GeV	< 70 GeV	< 70 GeV	> 145 GeV	> 145 GeV
$\Delta R_{b\bar{b}}$	< 1.2	< 1.2	$< 2.23 - 0.007 p_{\mathrm{T}}^{b\bar{b}}/\mathrm{GeV}$	$< 2.23 - 0.007 p_{\mathrm{T}}^{b\bar{b}}/\mathrm{GeV}$	> 1.5	> 1.6
$p_{\mathrm{T}}^{b\bar{b}}$	> 200 GeV	–	$\in (150, 250)$ GeV	> 80 GeV	> 250 GeV	> 180 GeV
$m_{\mathrm{top}}^{\mathrm{lep}}$	> 260 GeV	> 220 GeV	> 275 GeV	> 260 GeV	> 320 GeV	> 320 GeV
$\lvert\Delta y_{jj}\rvert$	$\in (3, 4.4)$	> 3	> 3	> 3	> 3	> 3
m_{jj}	–	$\in (400, 1000)$ GeV	–	> 500 GeV	–	> 500 GeV
$N_{\mathrm{jets}}^{\mathrm{veto}}$	–	< 2	–	< 1	–	< 2
p_{T}^{W}	–	< 350 GeV	–	–	> 250 GeV	> 250 GeV
m_{T}^{W}	–	–	–	< 200 GeV	–	–
p_{T}^{j1}	–	–	> 70 GeV	> 70 GeV	< 350 GeV	< 350 GeV

Systematic uncertainties considered for the electrons and muons include the trigger, reconstruction, identification, and isolation efficiency, in addition to the energy or momentum scale and resolution [21, 22]. For jets, uncertainties are considered on the energy scale and resolution [33], the vertex tagging efficiency [25, 26], and the b-tagging efficiency for b [28], c [34], and light jets [35]. Uncertainties on the momentum of all objects are propagated to $E_{\mathrm{T}}^{\mathrm{miss}}$; additional uncertainties are considered on the soft term [30] and on the trigger efficiency. Systematic uncertainties on the modeling of the main backgrounds are assessed by replacing the nominal MC predictions described previously with ones generated by MadGraph5_aMC@NLO [12] interfaced to Pythia8 [13], and, for $t\bar{t}$ and Wt, by using Herwig7 as an alternative parton shower. The treatment of overlap between $t\bar{t}$ and Wt is varied by using the alternative Diagram Subtraction (DS) scheme [36]. These uncertainties are symmetrized. Additionally, the renormalization and factorization scales are varied by a factor of two, and, for $t\bar{t}$ and Wt, other parameters sensitive to initial state radiation are also varied [37]. Because the normalization of these backgrounds is unconstrained in the likelihood fit, the systematic uncertainties affect only the relative contribution in each region. Uncertainties on the cross-section and acceptance of the smaller backgrounds are also considered, but have a small impact on the analysis. For the VBF WH signal, the renormalization and factorization scales, the PDF, and α_S are varied [38]. These result in an uncertainty in the SR yields of 10–15%.

Table 3 presents the normalization factors and background yields in each SR obtained from the fit, as well as the predicted signal and observed data yields. No significant pulls or constraints are observed on any nuisance parameters. Because the CRs are not fully pure in the target background, the normalization factors for these backgrounds are anti-correlated (for instance, a higher value of $k_{t\bar{t}}$ would imply more $t\bar{t}$ in the W CR, and therefore a lower k_W). This results in the uncertainty on the total predicted yield being smaller than the uncertainty on the individual components. The values of $k_{t\bar{t}}$ and k_W are close to unity, indicating good modeling from simulation. The values of k_{Wt} are significantly below 1, due to an excess of the MC prediction over the data in the Wt CRs. The phase space selected in this analysis is highly sensitive to the treatment of $t\bar{t}$-Wt overlap; using the alternative DS scheme, a MC deficit is seen in the Wt CRs, and values of k_{Wt} close to 3 are obtained. The difference between the baseline MC prediction and data is therefore smaller than the difference with an alternative prediction used to define the systematic uncertainty. Moreover, because the normalization of Wt is determined from the fit to data, the change in the measured signal strength using this prediction is less than 10% of the total uncertainty on the signal strength.

Table 3: Normalization factors, expected background and signal yields, and observed data yields in each signal region. The background yields are given after the fit to data, while the signal yields show both the pre-fit expectation and the fitted values. The VBF WH signal corresponds to the prediction with $\kappa_W = 1$, $\kappa_Z = -1$ for SR$^-$, and $\kappa_W = 1$, $\kappa_Z = 1$ for SR$^+_{\text{loose}}$ and SR$^+_{\text{tight}}$. The pre-fit expectation for $\kappa_W = 1$, $\kappa_Z = 1$ signal in SR$^-$ is 2.93 ± 0.35 events. The uncertainty on the total background is smaller than the sum of individual components due to correlations.

	Negative λ_{WZ}	Positive λ_{WZ}	
$k_{t\bar{t}}$	$0.88\,^{+0.29}_{-0.35}$	$0.91\,^{+0.19}_{-0.21}$	
k_W	$1.12\,^{+0.33}_{-0.24}$	$1.24\,^{+0.32}_{-0.23}$	
k_{Wt}	$0.32\,^{+0.39}_{-0.13}$	$0.36\,^{+0.43}_{-0.16}$	
μ	$-0.027\,^{+0.057}_{-0.061}$	$2.6\,^{+4.6}_{-4.5}$	
	SR$^-$	SR$^+_{\text{loose}}$	SR$^+_{\text{tight}}$
$t\bar{t}$	42 ± 19	162 ± 35	12.8 ± 4.5
W+jets	26 ± 13	80 ± 30	13.8 ± 7.3
Wt	$4.6\,^{+7.0}_{-4.6}$	$9\,^{+15}_{-9}$	$0.8\,^{+1.3}_{-0.8}$
Other background	5.4 ± 1.2	17.2 ± 4.5	2.6 ± 1.3
Total background	77.7 ± 8.4	269 ± 16	29.9 ± 5.9
VBF WH, pre-fit	285 ± 45	4.15 ± 0.50	2.30 ± 0.32
VBF WH, post-fit	-8 ± 16	10 ± 18	6 ± 10
Data	70	274	37

In SR$^-$, 70 data events are observed, compared to the expectation of 80.6 ± 8.4 assuming the SM, or 361 ± 46 in the $\kappa_W = 1$, $\kappa_Z = -1$ scenario[4]. Figure 2 shows confidence intervals in the (κ_Z, κ_W) plane. All values with opposite sign which are consistent with other Higgs boson measurements [2, 3] are excluded with significance greater than 8σ. From this, the sign of λ_{WZ} is determined to be positive.

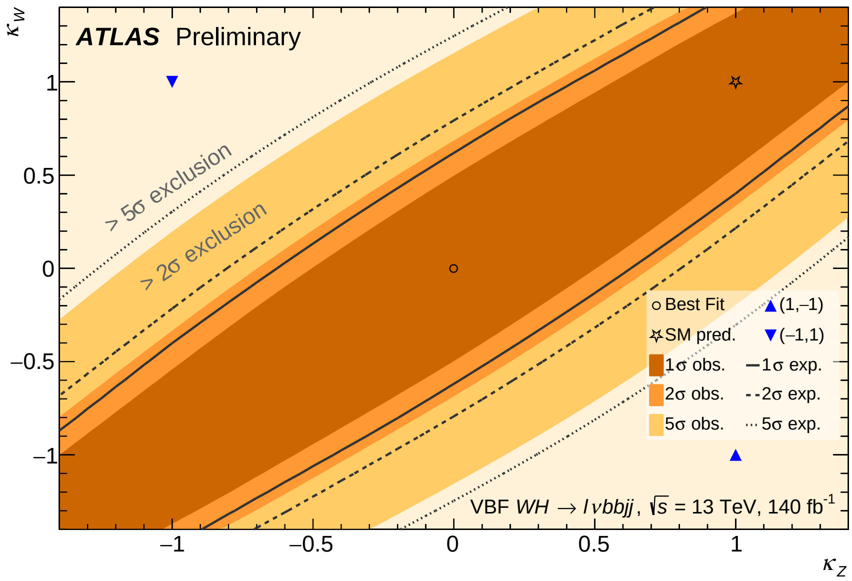

Figure 2: Fit results in the (κ_Z, κ_W) plane, using the negative λ_{WZ} analysis. Confidence intervals are constructed based on the log-likelihood ratio $\Lambda_{\rm LR} = -2\ln\left(L(\kappa_Z, \kappa_W)/L_{\rm max}\right)$, where $L_{\rm max}$ is the likelihood for the best fit point shown as an open circle. The 1σ, 2σ and 5σ intervals are defined by $\Lambda_{\rm LR}$ values smaller than 2.30, 6.18, and 28.7, respectively.

In the positive λ_{WZ} analysis, 274 (37) events are observed in $\text{SR}^+_{\text{loose}}$ ($\text{SR}^+_{\text{tight}}$), compared to an expected background of 269 ± 16 (29.9 ± 5.9), and a SM signal of 4.15 ± 0.50 (2.30 ± 0.32). The fitted value of the signal strength is $\mu = 2.6\,^{+2.6}_{-2.4}$ (stat.) ± 3.8 (syst.) $= 2.6\,^{+4.6}_{-4.5}$, indicating compatibility of the data with both the SM and the background-only hypotheses. The largest sources of systematic uncertainty come from the jet energy resolution and W+jets and $t\bar{t}$ modelling. An upper limit of 11.2 is set on the signal strength, compared to an expected limit of 9.4. The limit on the cross-section for SM-like VBF WH production times the branching ratio $H \to b\bar{b}$ is 383 fb.

In conclusion, the VBF WH process has been studied by the ATLAS experiment, using 140 fb^{-1} of pp collision data at $\sqrt{s} = 13$ TeV. Events with two b-jets, a charged lepton, and two additional jets with a large rapidity gap are considered. No excess of events is observed above the SM expectation. A limit is set on the cross-section for SM-like VBF WH production of 11.2 times the SM prediction, compared to an expected limit of 9.4. The W and Z boson couplings to the Higgs boson are determined to have the same sign, with previously un-excluded opposite-sign hypotheses now excluded at a significance greater than 8σ.

[4] This is less than the sum of signal and background in Table 3, due to the effect that signal contamination in the CRs would have on the background normalization factors.

Acknowledgments

We thank CERN for the very successful operation of the LHC, as well as the support staff from our institutions without whom ATLAS could not be operated efficiently.

We acknowledge the support of ANPCyT, Argentina; YerPhI, Armenia; ARC, Australia; BMWFW and FWF, Austria; ANAS, Azerbaijan; CNPq and FAPESP, Brazil; NSERC, NRC and CFI, Canada; CERN; ANID, Chile; CAS, MOST and NSFC, China; Minciencias, Colombia; MEYS CR, Czech Republic; DNRF and DNSRC, Denmark; IN2P3-CNRS and CEA-DRF/IRFU, France; SRNSFG, Georgia; BMBF, HGF and MPG, Germany; GSRI, Greece; RGC and Hong Kong SAR, China; ISF and Benoziyo Center, Israel; INFN, Italy; MEXT and JSPS, Japan; CNRST, Morocco; NWO, Netherlands; RCN, Norway; MEiN, Poland; FCT, Portugal; MNE/IFA, Romania; MESTD, Serbia; MSSR, Slovakia; ARRS and MIZŠ, Slovenia; DSI/NRF, South Africa; MICINN, Spain; SRC and Wallenberg Foundation, Sweden; SERI, SNSF and Cantons of Bern and Geneva, Switzerland; MOST, Taiwan; TENMAK, Türkiye; STFC, United Kingdom; DOE and NSF, United States of America. In addition, individual groups and members have received support from BCKDF, CANARIE, Compute Canada and CRC, Canada; PRIMUS 21/SCI/017 and UNCE SCI/013, Czech Republic; COST, ERC, ERDF, Horizon 2020 and Marie Skłodowska-Curie Actions, European Union; Investissements d'Avenir Labex, Investissements d'Avenir Idex and ANR, France; DFG and AvH Foundation, Germany; Herakleitos, Thales and Aristeia programmes co-financed by EU-ESF and the Greek NSRF, Greece; BSF-NSF and MINERVA, Israel; Norwegian Financial Mechanism 2014-2021, Norway; NCN and NAWA, Poland; La Caixa Banking Foundation, CERCA Programme Generalitat de Catalunya and PROMETEO and GenT Programmes Generalitat Valenciana, Spain; Göran Gustafssons Stiftelse, Sweden; The Royal Society and Leverhulme Trust, United Kingdom.

The crucial computing support from all WLCG partners is acknowledged gratefully, in particular from CERN, the ATLAS Tier-1 facilities at TRIUMF (Canada), NDGF (Denmark, Norway, Sweden), CC-IN2P3 (France), KIT/GridKA (Germany), INFN-CNAF (Italy), NL-T1 (Netherlands), PIC (Spain), ASGC (Taiwan), RAL (UK) and BNL (USA), the Tier-2 facilities worldwide and large non-WLCG resource providers. Major contributors of computing resources are listed in Ref. [39].

Appendix

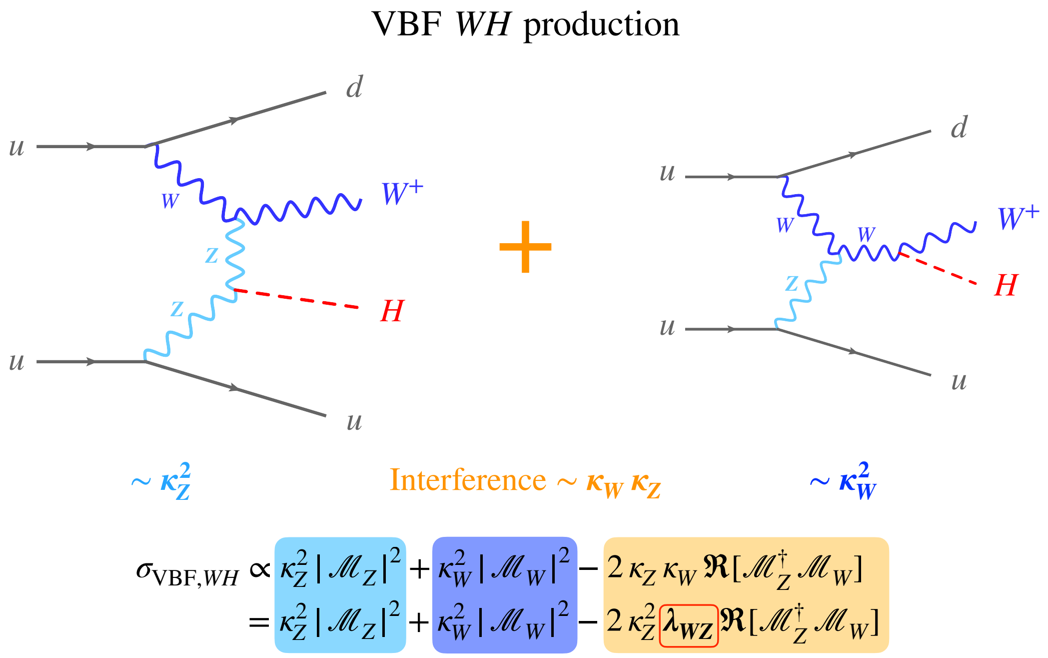

Figure 3: At leading order, VBF WH production is described by two classes of contributions, where the Higgs boson either interacts with a Z boson or with a W boson. Representative diagrams of these two kinds of contributions are shown above. The equations present the tree-level contributions to the production cross section, where coupling modifiers have been introduced for the HZ and HW vertices and the contributions from the two classes of diagrams are grouped into $\mathcal{M}_Z$ and $\mathcal{M}_W$. The interference term shown in the orange box gives a significant contribution, which is destructive in the SM ($\kappa_W = \kappa_Z = \lambda_{WZ} = 1$) but becomes constructive in case λ_{WZ} takes on negative values.

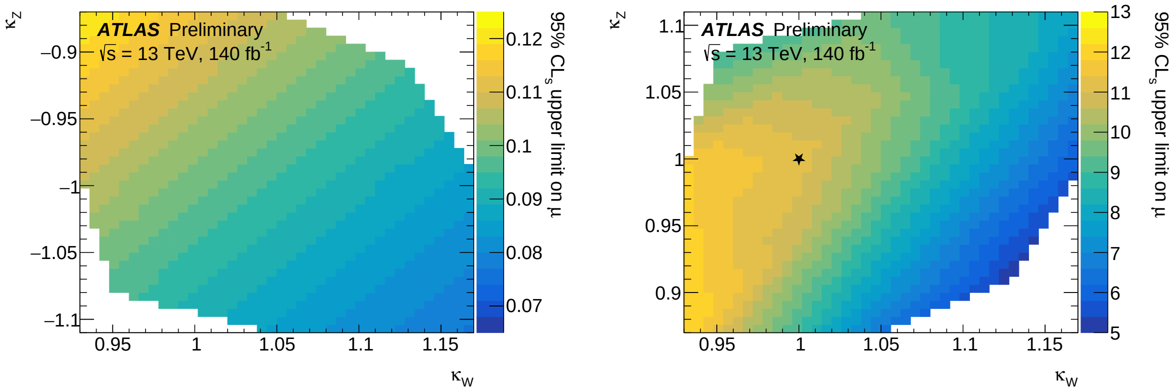

Figure 4: Exclusion limits at 95% $\mathrm{CL_s}$ on the signal strength for VBF WH production for different values of κ_W and κ_Z. Negative values of λ_{WZ} are on the left, and positive values are on the right. The Standard Model is indicated with a star. The white regions are excluded at greater than 95% confidence level by other ATLAS Higgs boson measurements [2], and do not have simulated signal predictions.

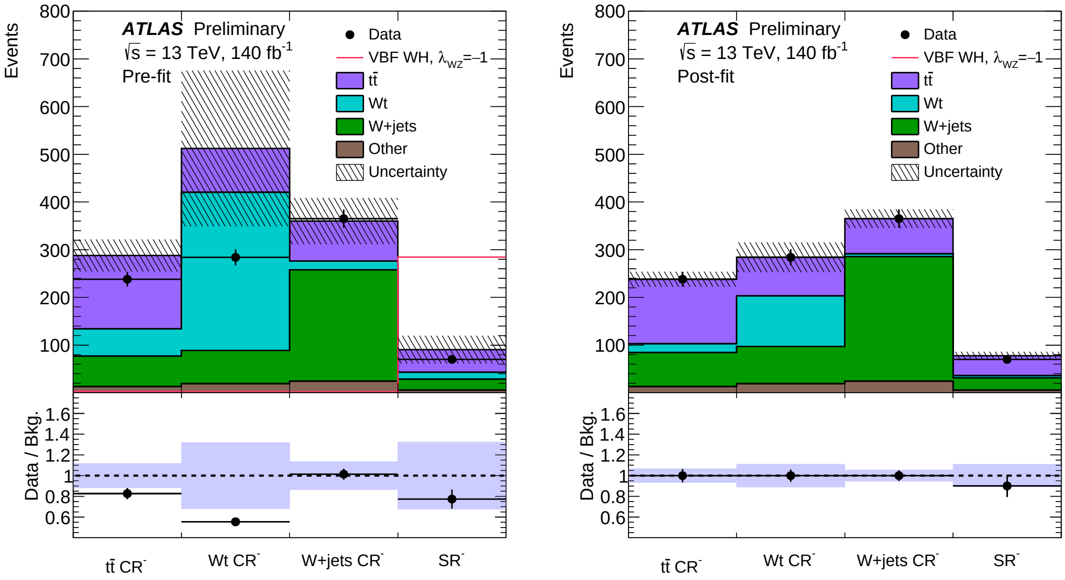

Figure 5: Data compared to the background prediction in each region of the negative λ_{WZ} analysis, before (left) and after (right) the fit to data. The signal prediction with $\kappa_W = +1$, $\kappa_Z = -1$ is shown overlaid in the pre-fit plot. The fitted signal strength is $\hat{\mu} = -0.027$, corresponding to -8 events. This contribution is not shown in the figure. The predicted signal yield with $\kappa_W = +1$, $\kappa_Z = +1$ in SR$^-$ is 2.93 events, which is also not shown in the figure. The shaded bands represent the total pre- or post-fit uncertainty on the prediction. The pre-fit uncertainty does not include the normalization of the main backgrounds, which is unconstrained in the fit.

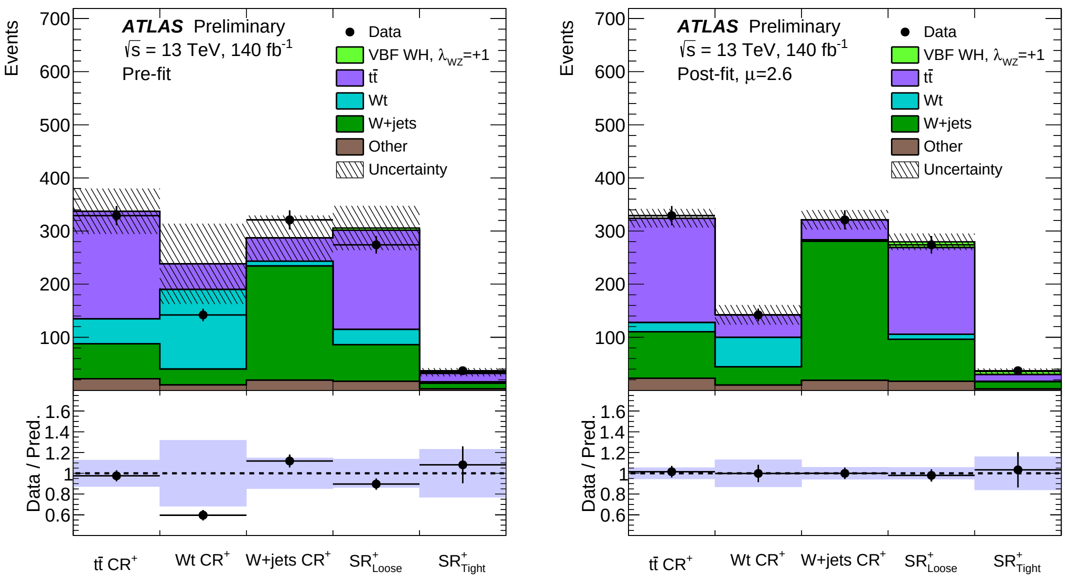

Figure 6: Data compared to the SM prediction in each region of the positive λ_{WZ} analysis, before (left) and after (right) the fit to data. The shaded bands represent the total pre- or post-fit uncertainty on the prediction. The pre-fit uncertainty does not include the normalization of the main backgrounds, which is unconstrained in the fit.

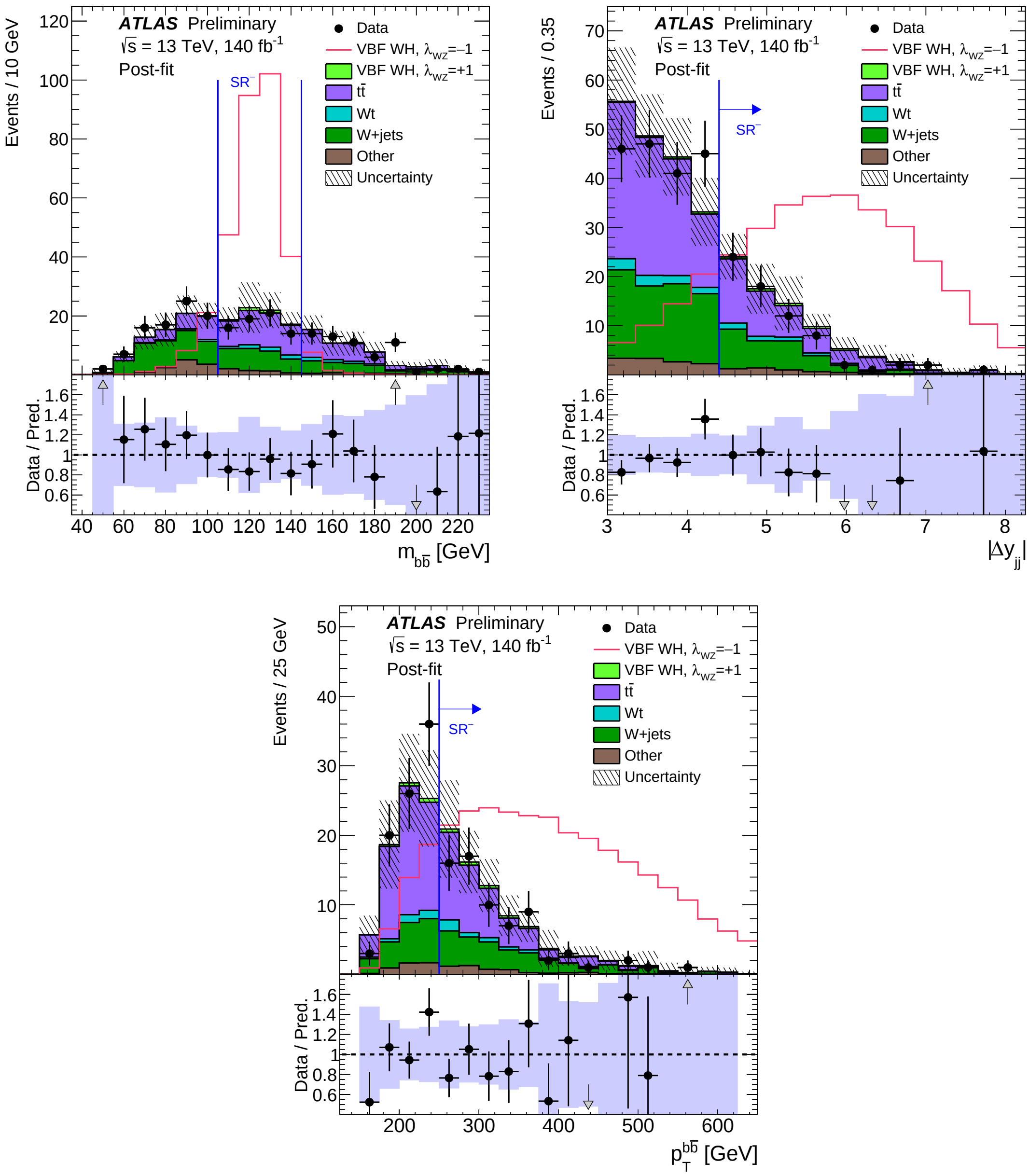

Figure 7: Data compared to the SM prediction for $m_{b\bar{b}}$, $|\Delta y_{jj}|$, and $p_{\mathrm{T}}^{b\bar{b}}$ in the negative λ_{WZ} analysis. The background yields are scaled to the post-fit prediction. The SM signal with $\kappa_W = +1$, $\kappa_Z = +1$ is shown as part of the stacked prediction, while the BSM signal with $\kappa_W = +1$, $\kappa_Z = -1$ is presented separately. For each figure, all of the cuts used to define SR$^-$ are applied, except for the cut on the represented variable. These cuts are indicated with a blue line. The shaded bands represent the total post-fit uncertainty on the prediction.

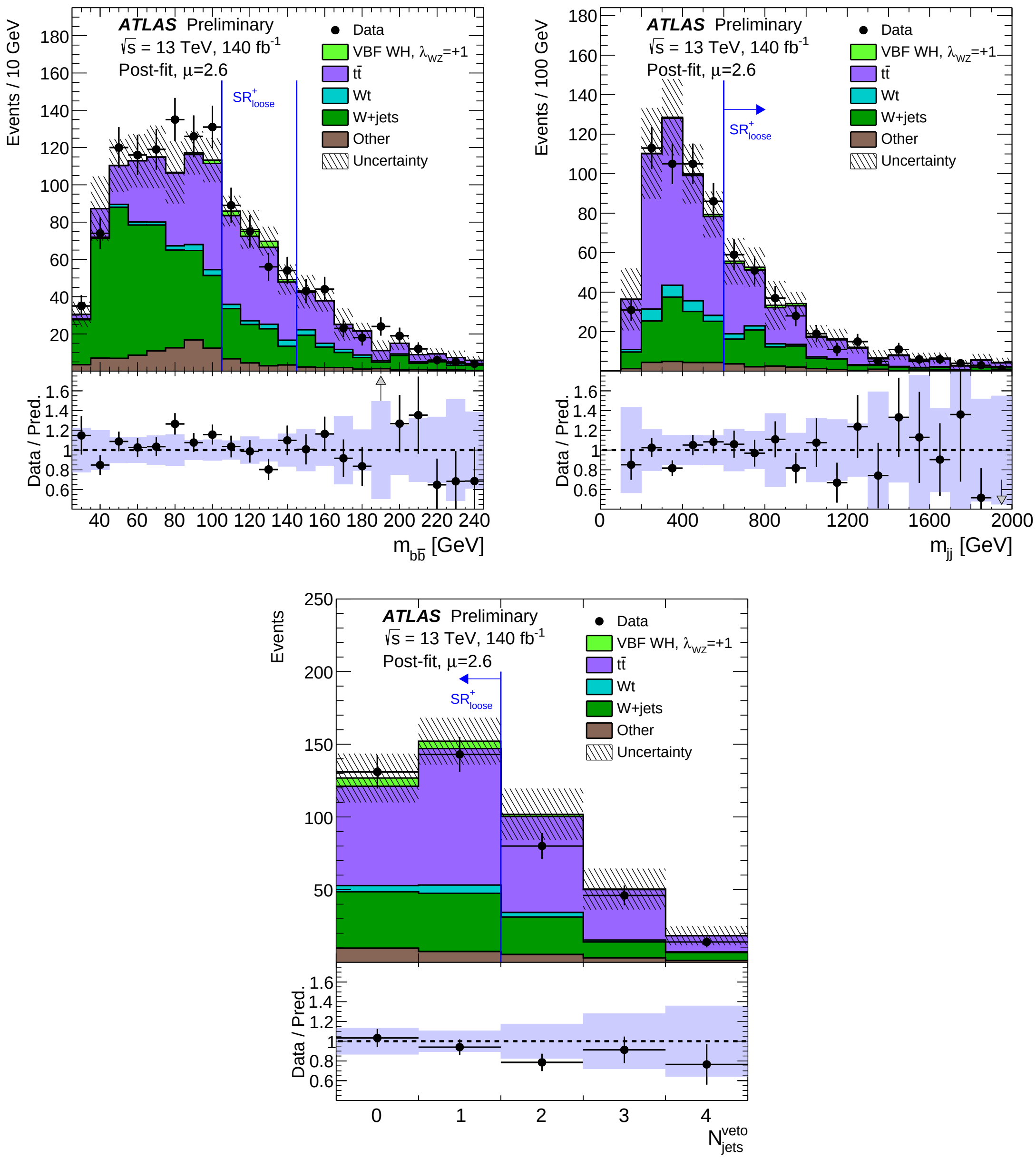

Figure 8: Data compared to the SM prediction for $m_{b\bar{b}}$, m_{jj}, and $N^{\text{veto}}_{\text{jets}}$ in the positive λ_{WZ} analysis. The background yields are scaled to the post-fit prediction, while the signal is scaled to the fitted signal strength $\mu = 2.6$. For each figure, all of the cuts used to define $\text{SR}^{+}_{\text{loose}}$ are applied, except for the cut on the represented variable. These cuts are indicated with a blue line. The shaded bands represent the total post-fit uncertainty on the prediction.

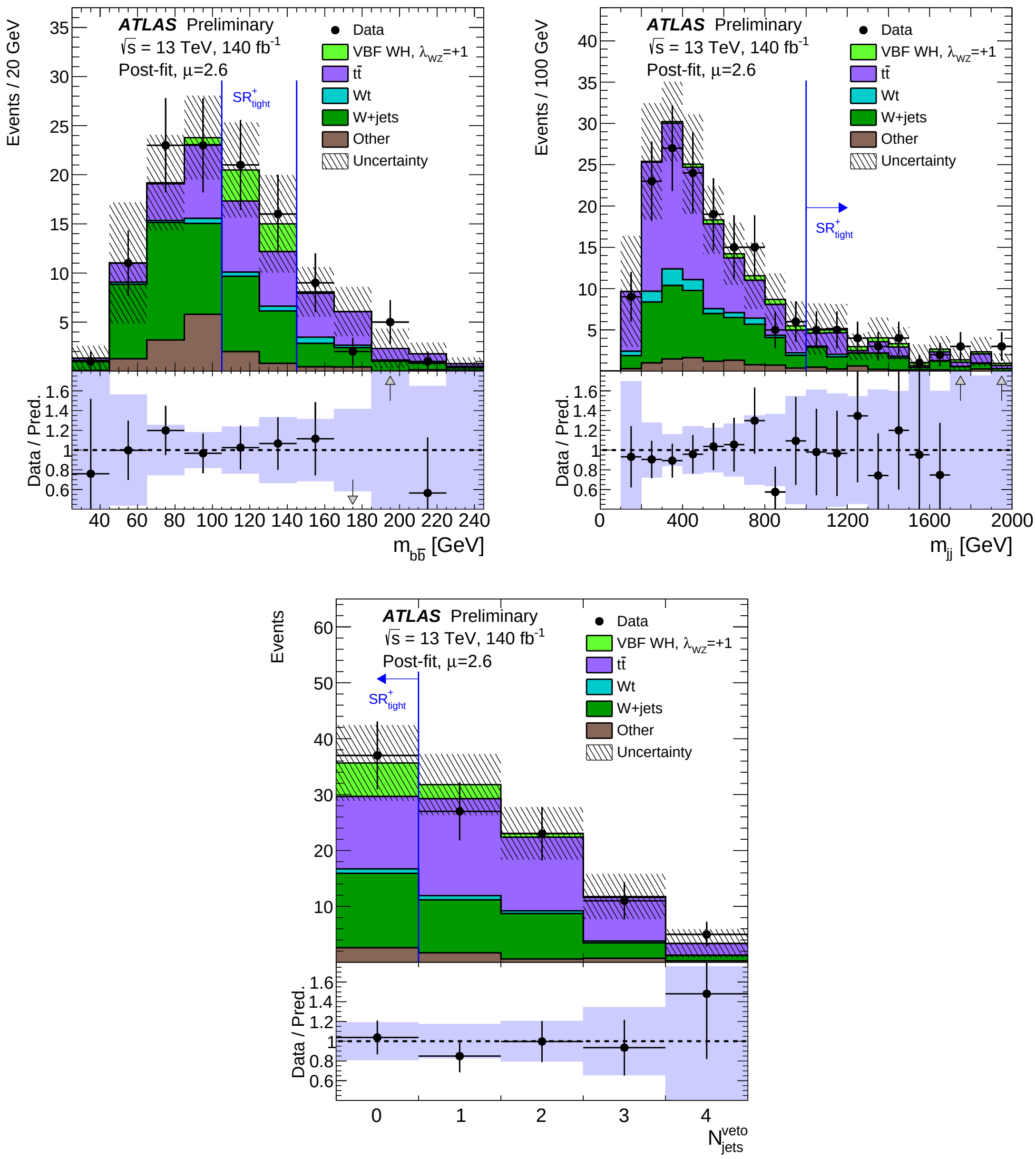

Figure 9: Data compared to the SM prediction for $m_{b\bar{b}}$, m_{jj}, and $N_{\text{jets}}^{\text{veto}}$ in the positive λ_{WZ} analysis. The background yields are scaled to the post-fit prediction, while the signal is scaled to the fitted signal strength $\mu = 2.6$. For each figure, all of the cuts used to define $\text{SR}^{+}_{\text{tight}}$ are applied, except for the cut on the represented variable. These cuts are indicated with a blue line. The shaded bands represent the total post-fit uncertainty on the prediction.

Uncertainty source	$\Delta\mu$
$t\bar{t}$ modelling	$\pm\,0.033$
Jet energy resolution	$\pm\,0.027$
Wt modelling	$\pm\,0.012$
Jet energy scale	$\pm\,0.011$
MC statistical uncertainty	$\pm\,0.006$
W+jets modelling	$\pm\,0.004$
Signal modelling	$\pm\,0.004$
Flavor tagging	$\pm\,0.002$
Jet vertex tagging	$\pm\,0.002$
$E_{\mathrm{T}}^{\mathrm{miss}}$ scale and trigger efficiency	$\pm\,0.001$
Luminosity and pileup reweighting	$\pm\,0.001$
Other background modelling	$\pm\,0.001$
Lepton scale and efficiency	<0.001
Total systematic	$\pm\,0.049$
Normalization factors	$\pm\,0.021$
Total statistical	$\pm\,0.032$
Total uncertainty	$\pm\,0.059$

Table 4: Contribution of different sources of uncertainty to the total uncertainty on μ, in the negative λ_{WZ} analysis. In the case of asymmetric uncertainties, the average of the positive and negative variations is given.

Uncertainty source	$\Delta\mu$
Jet energy resolution	$\pm\,2.4$
W+jets modelling	$\pm\,2.1$
$t\bar{t}$ modelling	$\pm\,1.3$
MC statistical uncertainty	$\pm\,0.9$
Other background modelling	$\pm\,0.6$
Jet energy scale	$\pm\,0.5$
Wt modelling	$\pm\,0.3$
Signal modelling	$\pm\,0.3$
$E_{\mathrm{T}}^{\mathrm{miss}}$ scale and trigger efficiency	$\pm\,0.3$
Luminosity and pileup reweighting	$\pm\,0.1$
Flavor tagging	$\pm\,0.1$
Jet vertex tagging	$\pm\,0.1$
Lepton scale and efficiency	<0.1
Total systematic	$\pm\,3.8$
Normalization factors	$\pm\,1.9$
Total statistical	$\pm\,2.4$
Total uncertainty	$\pm\,4.5$

Table 5: Contribution of different sources of uncertainty to the total uncertainty on μ, in the positive λ_{WZ} analysis. In the case of asymmetric uncertainties, the average of the positive and negative variations is given.

References

[1] J. R. Andersen et al., *Handbook of LHC Higgs Cross Sections: 3. Higgs Properties*, (2013), ed. by S. Heinemeyer, C. Mariotti, G. Passarino, and R. Tanaka, arXiv: 1307.1347 [hep-ph] (cit. on p. 2).

[2] ATLAS Collaboration, *A detailed map of Higgs boson interactions by the ATLAS experiment ten years after the discovery*, Nature **607** (2022) 52, arXiv: 2207.00092 [hep-ex] (cit. on pp. 2, 7, 10).

[3] CMS Collaboration, *A portrait of the Higgs boson by the CMS experiment ten years after the discovery*, Nature **607** (2022) 60, arXiv: 2207.00043 [hep-ex] (cit. on pp. 2, 7).

[4] I. Low and J. Lykken, *Revealing the Electroweak Properties of a New Scalar Resonance*, JHEP **10** (2010) 053, arXiv: 1005.0872 [hep-ph] (cit. on p. 2).

[5] H. Georgi and M. Machacek, *Doubly charged Higgs bosons*, Nuclear Physics B **262** (1985) 463, ISSN: 0550-3213, URL: https://www.sciencedirect.com/science/article/pii/0550321385903256 (cit. on p. 2).

[6] D. Stolarski and Y. Wu, *Tree-level interference in vector boson fusion production of Vh*, Physical Review D **102** (2020) (cit. on pp. 2, 3).

[7] Y. Chen, J. Lykken, M. Spiropulu, D. Stolarski, and R. Vega-Morales, *Golden Probe of Electroweak Symmetry Breaking*, Phys. Rev. Lett. **117** (2016) 241801, arXiv: 1608.02159 [hep-ph] (cit. on p. 2).

[8] C.-W. Chiang, X.-G. He, and G. Li, *Measuring the ratio of HWW and HZZ couplings through W^+W^-H production*, JHEP **08** (2018) 126, arXiv: 1805.01689 [hep-ph] (cit. on p. 2).

[9] ATLAS Collaboration, *Luminosity determination in pp collisions at $\sqrt{s} = 13$ TeV using the ATLAS detector at the LHC*, (2022), arXiv: 2212.09379 [hep-ex] (cit. on p. 2).

[10] ATLAS Collaboration, *The ATLAS Experiment at the CERN Large Hadron Collider*, JINST **3** (2008) S08003 (cit. on p. 2).

[11] ATLAS Collaboration, *The ATLAS Collaboration Software and Firmware*, ATL-SOFT-PUB-2021-001, 2021, URL: https://cds.cern.ch/record/2767187 (cit. on p. 3).

[12] J. Alwall et al., *The automated computation of tree-level and next-to-leading order differential cross sections, and their matching to parton shower simulations*, JHEP **07** (2014) 079, arXiv: 1405.0301 [hep-ph] (cit. on pp. 3, 6).

[13] T. Sjöstrand et al., *An introduction to PYTHIA 8.2*, Comput. Phys. Commun. **191** (2015) 159, arXiv: 1410.3012 [hep-ph] (cit. on pp. 3, 6).

[14] The NNPDF Collaboration, R. D. Ball, et al., *Parton distributions for the LHC run II*, JHEP **04** (2015) 040, arXiv: 1410.8849 [hep-ph] (cit. on p. 3).

[15] S. Frixione, G. Ridolfi, and P. Nason, *A positive-weight next-to-leading-order Monte Carlo for heavy flavour hadroproduction*, JHEP **09** (2007) 126, arXiv: 0707.3088 [hep-ph] (cit. on p. 3).

[16] P. Nason, *A new method for combining NLO QCD with shower Monte Carlo algorithms*, JHEP **11** (2004) 040, arXiv: hep-ph/0409146 (cit. on p. 3).

[17] S. Frixione, E. Laenen, P. Motylinski, C. White, and B. R. Webber, *Single-top hadroproduction in association with a W boson*, JHEP **07** (2008) 029, arXiv: 0805.3067 [hep-ph] (cit. on p. 3).

[18] E. Bothmann et al., *Event generation with Sherpa 2.2*, SciPost Phys. **7** (2019) 034, arXiv: 1905.09127 [hep-ph] (cit. on p. 3).

[19] L. Lönnblad, *Correcting the Colour-Dipole Cascade Model with Fixed Order Matrix Elements*, JHEP **05** (2002) 046, arXiv: hep-ph/0112284 (cit. on p. 3).

[20] G. Luisoni, P. Nason, C. Oleari, and F. Tramontano, *$HW^{\pm}/HZ$ + 0 and 1 jet at NLO with the POWHEG BOX interfaced to GoSam and their merging within MiNLO*, JHEP **10** (2013) 083, arXiv: 1306.2542 [hep-ph] (cit. on p. 3).

[21] ATLAS Collaboration, *Electron and photon performance measurements with the ATLAS detector using the 2015–2017 LHC proton–proton collision data*, JINST **14** (2019) P12006, arXiv: 1908.00005 [hep-ex] (cit. on pp. 3, 5).

[22] ATLAS Collaboration, *Muon reconstruction and identification efficiency in ATLAS using the full Run 2 pp collision data set at $\sqrt{s} = 13$ TeV*, Eur. Phys. J. C **81** (2021) 578, arXiv: 2012.00578 [hep-ex] (cit. on pp. 4, 5).

[23] ATLAS Collaboration, *Jet reconstruction and performance using particle flow with the ATLAS Detector*, Eur. Phys. J. C **77** (2017) 466, arXiv: 1703.10485 [hep-ex] (cit. on p. 4).

[24] M. Cacciari, G. P. Salam, and G. Soyez, *The anti-k_t jet clustering algorithm*, JHEP **04** (2008) 063, arXiv: 0802.1189 [hep-ph] (cit. on p. 4).

[25] ATLAS Collaboration, *Tagging and suppression of pileup jets with the ATLAS detector*, ATLAS-CONF-2014-018, 2014, URL: https://cds.cern.ch/record/1700870 (cit. on pp. 4, 5).

[26] ATLAS Collaboration, *Forward jet vertex tagging using the particle flow algorithm*, ATL-PHYS-PUB-2019-026, 2019, URL: https://cds.cern.ch/record/2683100 (cit. on pp. 4, 5).

[27] ATLAS Collaboration, *Optimisation and performance studies of the ATLAS b-tagging algorithms for the 2017-18 LHC run*, ATL-PHYS-PUB-2017-013, 2017, URL: https://cds.cern.ch/record/2273281 (cit. on p. 4).

[28] ATLAS Collaboration, *ATLAS b-jet identification performance and efficiency measurement with $t\bar{t}$ events in pp collisions at $\sqrt{s} = 13$ TeV*, Eur. Phys. J. C **79** (2019) 970, arXiv: 1907.05120 [hep-ex] (cit. on pp. 4, 5).

[29] ATLAS Collaboration, *Evidence for the $H \rightarrow b\bar{b}$ decay with the ATLAS detector*, JHEP **12** (2017) 024, arXiv: 1708.03299 [hep-ex] (cit. on p. 4).

[30] ATLAS Collaboration, *Performance of missing transverse momentum reconstruction with the ATLAS detector using proton–proton collisions at $\sqrt{s} = 13$ TeV*, Eur. Phys. J. C **78** (2018) 903, arXiv: 1802.08168 [hep-ex] (cit. on pp. 4, 6).

[31] M. G. Kendall and A. Stuart, *The Advanced Theory of Statistics, Volume 2: Inference and Relationship*, London: Charles Griffin, 1961 (cit. on p. 5).

[32] G. Cowan, K. Cranmer, E. Gross, and O. Vitells,
Asymptotic formulae for likelihood-based tests of new physics, Eur. Phys. J. C **71** (2011) 1554,
arXiv: 1007.1727 [physics.data-an] (cit. on p. 5), Erratum: Eur. Phys. J. C **73** (2013) 2501.

[33] ATLAS Collaboration, *Jet energy scale and resolution measured in proton–proton collisions at* $\sqrt{s} = 13$ *TeV with the ATLAS detector*, Eur. Phys. J. C **81** (2020) 689,
arXiv: 2007.02645 [hep-ex] (cit. on p. 5).

[34] ATLAS Collaboration, *Measurement of the c-jet mistagging efficiency in* $t\bar{t}$ *events using* pp *collision data at* $\sqrt{s} = 13$ *TeV collected with the ATLAS detector*, Eur. Phys. J. C **82** (2022) 95,
arXiv: 2109.10627 [hep-ex] (cit. on p. 5).

[35] ATLAS Collaboration,
Calibration of the light-flavour jet mistagging efficiency of the b-tagging algorithms with Z+jets events using 139 *fb*$^{-1}$ *of ATLAS proton–proton collision data at* $\sqrt{s} = 13$ *TeV*, (2023),
arXiv: 2301.06319 [hep-ex] (cit. on p. 5).

[36] C. D. White, S. Frixione, E. Laenen, and F. Maltoni, *Isolating Wt production at the LHC*,
JHEP **2009** (2009) 074, arXiv: 0908.0631 (cit. on p. 6).

[37] ATLAS Collaboration,
Study of top-quark pair modelling and uncertainties using ATLAS measurements at $\sqrt{s} = 13$ *TeV*,
ATL-PHYS-PUB-2020-023, 2020, URL: https://cds.cern.ch/record/2730443 (cit. on p. 6).

[38] J. Butterworth et al., *PDF4LHC recommendations for LHC Run II*, J. Phys. G **43** (2016) 023001,
arXiv: 1510.03865 [hep-ph] (cit. on p. 6).

[39] ATLAS Collaboration, *ATLAS Computing Acknowledgements*, ATL-SOFT-PUB-2021-003, 2021,
URL: https://cds.cern.ch/record/2776662 (cit. on p. 8).